Micro-patterns of gold nanoparticles assembled by photovoltaic optoelectronic tweezers: application to plasmonic fluorescence enhancement

IRIS ELVIRA,[1] ANDRÉS PUERTO,[1,2] GLADYS MÍNGUEZ-VEGA,[3] (iD)
ADRIÁN RODRÍGUEZ-PALOMO,[4] ALEJANDRO GÓMEZ-TORNERO,[1]
ANGEL GARCÍA-CABAÑES,[1,2] (iD)
AND MERCEDES CARRASCOSA[1,2,*] (iD)

[1]*Departamento de Física de Materiales, Universidad Autónoma de Madrid, ES-28049 Madrid, Spain*
[2]*Instituto Universitario Nicolás Cabrera, Universidad Autónoma de Madrid, ES-28049 Madrid, Spain*
[3]*Institut de Noves Tecnologies de la Imatge, Universitat Jaume I, ES-12071 Castelló, Spain*
[4]*Departamento de Química Inorgánica y Bioinorgánica, Universidad Complutense de Madrid and Instituto de Investigación Sanitaria Hospital 12 de Octubre, ES-28040 Madrid, Spain*
*m.carrascosa@uam.es

Abstract: Noble metal nanostructures are well-known for their ability to increase the efficiency of different optical or physical phenomena due to their plasmonic behavior. This work presents a simple strategy to obtain Au plasmonic patterns by optically induced nanoparticle assembly and its application as fluorescence enhancement platforms. This strategy is based on the so-called photovoltaic optoelectronic tweezers (PVOT) being the first time they are used for fabricating Au periodic micro-patterns. Fringe patterns with a sub-structure of aggregates, assembled from individual spherical nanoparticles of 3.5 or 170 nm diameters, are successfully obtained. The spatial distribution of the aggregates is controlled with micrometric accuracy and the patterns can be arranged over large-scale active areas (tens of mm^2). The outcome for the ultra-small (3.5 nm) particles is particularly relevant because this diameter is the smallest one manipulated by PVOT so far. Testing experiments of plasmonic fluorescence enhancement show that the 170-nm patterns present a much better plasmonic behavior. For the 170-nm platform they reveal a 10-fold enhancement factor in the fluorescence of Rhodamine-B dye molecules and a 3-fold one for tagged DNA biomolecules. Hence, the results suggest that these latter plasmonic platforms are good candidates for efficient bio-imaging and biosensing techniques, among other applications.

1. Introduction

Metallic nanoparticles (NPs) are very well-known for their interesting optical properties at the nanoscale [1–5]. In this context, the noble metals Au and Ag are the protagonists. Particularly, Au NPs usually offer an intense plasmonic response extended along the VIS-NIR, overlapping with the biological transparency windows when suitable designed [6–8]. In addition, they are highly inert (which makes them relatively biocompatible), colloidally stable, and easy to be functionalized. All of this makes the Au NPs suitable for applications in the field of biotechnology, being able to participate in labelling, delivering, heating, or sensing experiments [9–11].

The light extinguished by a NP is caused by two phenomena: scattering and absorption (the latest usually converted to non-radiative processes). When it concerns the metallic NPs, their size plays a relevant role on their plasmonic behavior [12]. On the one hand, metallic NPs with larger sizes (usually > 50–100 nm) are efficient scatters at the wavelength of the plasmonic resonance (LSPR, localized surface plasmon resonance). Therefore, they have been mostly used in applications in which the enhancement of the local electric field is exploitable such as in

fluorescence (FL) microscopy, surface enhanced Raman scattering (SERS), light collection in solar cells, and frequency conversion processes, among others [13–16]. On the other hand, for metallic NPs with sizes of only some tens of nanometers or even less, the scattering cross-section decreases faster than the absorption cross-section, conferring them good capabilities as efficient heaters when excited at the LSPR. Thus, there are typically used in photo-acoustic imaging or photothermal therapy [6,11]. However, not only individual NPs offer profitable plasmonic properties. There is also a growing interest in the exploitation of the plasmonic effects of more complex structures. They are used to be assembled by sets of individual NPs, sometimes called plasmonic nanoparticle networks (PNNs) [16–18]. This kind of structures have demonstrated to be good as light and heat concentrators [19].

Some of the techniques proposed for the fabrication of complex metallic structures on top of a surface are optical tweezers (OT), electron or ion beam lithography, spin casting of polymer films, and more recently nanoimprint lithography, to name a few [20–22]. All these techniques boast to provide a high level of control in the manipulation, which makes them suitable for the fabrication of highly ordered PNNs. However, they tend to be time-consuming when a high number of particles has to be manipulated and the particle size (or even the metallic nature as happens with the OT) is often a handicap. Furthermore, the manufacturing costs are also high, preventing the scalability to the industry. An alternative simpler patterning technique is based in self-assembly of NPs along the striations generated in polymer films [23,24]. Remarkable pattern resolution has been recently achieved [25]. However, only fringe patterns with a radial symmetry have been reported [23–25]. Conversely, PVOT is a kind of optoelectronic technique with high patterning flexibility that has demonstrated to be powerful for massive manipulation and trapping and patterning of dielectric and metallic NPs [26,27]. 1D and 2D arbitrary patterns can be assembled taking advantage of the patterning capabilities of light images. Moreover, erasure and reconfiguration of the patterns have been recently reported [28]. The PVOT is based on the bulk photovoltaic (PV) effect that presents some ferroelectric crystals such as the Fe-doped LiNbO$_3$ (Fe:LiNbO$_3$). This effect generates a light-induced bulk electric field that extends outside the crystal acting on nearby particles. The technique allows manipulating both, charged objects (by electrophoresis, EP) or neutral polarizable particles (by dielectrophoresis, DEP) [29], with different geometry, size, and nature [30–33]. Moreover, the possibility to fabricate a variety of combinatorial 1D and 2D patterns with different kind of particles has been recently reported [34]. In summary, PVOT is a very flexible, easy to implement, and cost-effective technique. Typically, this tool has been employed together with particles of sizes in the range of 40 µm - 25 nm, enable developing applications in the fields of optofluidics, biophysics, and photonics [35–39]. Recently, the authors of this work demonstrated the possibility to fabricate by PVOT Ag micro-patterns with application for dye FL plasmonic enhancement [40]. To our knowledge, this work also reports the minimum particle size (25 nm diameter Ag NPs) used with the PVOT so far.

In this work, we report for the first time the manipulation, trapping, and assembling of Au nanoparticles by using PVOT, exploring the challenge to obtain efficient plasmonic platforms. Two markedly different NP sizes (170 and 3.5-nm diameters) have been utilized. The latest NPs size (often named Ultra-Small NPs, USNPs) is the smallest particle size assembled by PVOT so far overpassing the previous record of 25 nm. High quality metallic fringe micro-structures have been successfully fabricated. The sub-structure of the fringes has been morphologically characterized by scanning electron microscopy (SEM). In turn, the plasmonic response has been investigated by reflectance spectroscopy, discussing it in connection with the morphological results. The micrometric patterns assembled by the Au 170 nm NPs, that show a broad plasmonic spectral response, have been tested as active slides for increasing the FL emission of Rhodamine-B (RB) molecules. Finally, to show the platform bio-technological potential, an application consisting of enhancing the FL intensity of tagged DNA biomolecules has been demonstrated.

2. Synthesis and features of the Au NPs

Non-commercial Au NPs with different sizes have been employed in order to assemble the metallic micro-patterns. To fabricate the NPs, two different approaches have been used. On the one hand, Au spherical NPs with 170 nm nominal diameter were synthesized by Pulsed Laser Ablation in Liquids (PLAL) as described in the work of Zhang *et* al. [41]. The fabrication procedure consists of irradiating the surface of an Au solid target surrounded by hexane with a focused pulsed laser beam. As a pulsed laser, we employed a Ti:sapphire laser with 30 fs full width at half maximum pulses at the central wavelength of 800 nm, and a repetition rate of 1 kHz. The laser beam with a diameter of 6 mm (at $1/e^2$), and an average power of 150 mW was focused onto the surface of the gold target with a spherical convex 75 mm lens. The Au sample submerged in hexane was placed at the bottom of a quartz cuvette, attached to a two-dimensional motion-controlled stage moving at a constant speed of 0.45 mm/s in the focus plane perpendicular to the laser beam, following a stair-like pattern. In order to avoid non-linear effects in the liquid and increase the production, the simultaneous spatial and temporal focusing technique where employed [42]. The size distribution and shape were characterized by dynamic light scattering (DLS) with a NP analyzer (Zetasizer Nano ZS, Malvern Instruments), obtaining a spherical shape and an average diameter of 166 ± 25 nm. These NPs demonstrated an essentially neutral behavior in the context of the PVOT, even although the fabrication method induced a residual charge of them. The suspension showed a disaggregated and stable NP behavior in the short and long-time scales, demonstrating the good capabilities of this synthesis method based on a physical approach. The LSPR of the NPs suspended on the colloid was characterized with a spectrophotometer, exhibiting a resonance centered at 570 nm.

On the other hand, Au USNPs with nominal 3.5 nm diameter were synthesized by using a chemical approach based on the reported work of Deraedt *et* al. [43]. Firstly, a stock solution of $HAuCl_4$ (5 μM, ($\geq$ 99.9%, Sigma Aldrich) in Milli-Q water was prepared. Hereafter, a 1.2 mL of a freshly solution of $NaBH_4$ made in Milli-Qwater (50 mM, > 96%, Sigma Aldrich) was added to 10 mL of the Au solution, placed in a glass vial and put under vigorous stirring at room temperature for 5 minutes. After that time, the stirrer was switched off and the solution was rested for 30 minutes. The resulting particles (3.5 nm, 0.4 mM) were coated with negatively charged borate ions and being the aqueous colloid stable. Since the PVOT technique required the NPs immersed in a polar medium, an additional final step consisting in the transference of NPs from the aqueous colloid to hexane was needed. Thus, after the synthesis, the NP solution was diluted with 3.9 mL of acetone (> 99.5%, Sigma Aldrich) and 3.3 mL of a stock solution of hexane ($\geq$ 99%, Sigma Aldrich) containing 1-Dodecanethiol ($\geq$ 98%, Sigma Aldrich). The ratio of Dodecanethiol molecules was set to 10% of the Au concentration, as described in the procedure reported by Martin *et* al. [44]. All glassware was carefully cleaned and rinsed with a mixture of HNO_3 and HCl (1:3) before use. Transmission Electron Microscopy (TEM) was performed in order to characterize the morphology and size of the Au USNPs. They revealed a spherical shape and an average diameter 3.5 nm and the LSPR for the particle colloid in hexane is centered at 510 nm.

3. Optoelectronic assembly of the Au nanoparticle patterns

To assemble the nanoparticle patterns we have employed the PVOT following a simple procedure that includes three sequential steps (a scheme is depicted in Fig. 1): i) illumination of the active Fe:LiNbO$_3$ with a suitable non-homogeneous fringe light profile in order to generate de inner and outer PV fields, ii) approaching of the Au NPs to the surface of the substrate, and iii) NP trapping and arrangement in order to build the pattern. The last two steps are caused by the action of the electric (DEP or EP) forces. Two substrate orientations (shown in Fig. 2) with the ferroelectric polar *c*-axis perpendicular (*z*-cut) or parallel (*x*-cut) to the active surface are used leading to quite

different particle patterns [45]. The fundamentals of the technique can be found in two recent reviews [26,27].
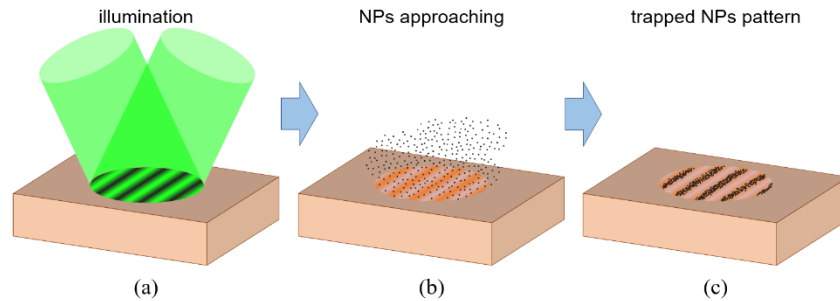

illumination   NPs approaching   trapped NPs pattern

(a)   (b)   (c)

Fig. 1. Scheme for the PVOT operation using the sequential method: (a) Illumination of the PV substrate (in this case a *z*-cut substrate illuminated with a sinusoidal light profile), (b) NP approaching to the substrate under DEP or EP forces, and (c) resulting NP pattern.
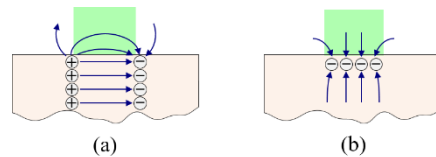

(a)   (b)

Fig. 2. Schematic of the two main configurations for the PV substrate showing the photo-induce electric field lines for single beam homogeneous illumination: (a) polar axis parallel to the active photovoltaic substrate (*x*-cut), and (b) polar axis normal to the active photovoltaic substrate (*z*-cut).

The Fe:LiNbO$_3$ crystals employed were highly doped with Fe (0.25% mol) and had 1 mm thickness (Hangzhou Freqcontrol Electronic Technology and Photox). They were illuminated for generating the PV fields with a frequency-doubled Nd:YAG laser operating at $\lambda = 532$ nm (Verdi V-5, Coherent). Two types of fringe periodic patterns have been successfully fabricated. On the one hand, fringe patterns with periodicity (Λ) and particle fringe thickness (δ) in the range of hundreds of µm were fabricated over *z*-cut Fe:LiNbO$_3$ substrates by using a spatial light modulator to generate the light intensity profile. On the other hand, patterns with very thin fringes (near 2 µm width), were obtained by illuminating *x*-cut substrates with a high contrast sinusoidal interference pattern produced by two laser beams of equal light intensity. In both kind of experiments, the substrates were illuminated with an intensity of $I \sim 1\text{-}100$ mW/cm^2 for ~ 10 minutes. The Au spherical NPs with the two different diameters, 3.5 and 170 nm were deposited on the Fe:LiNbO$_3$ from a hexane colloid containing them by immersing the substrate during 30 s.

We have selected three of the most representative Au patterns to carry out a detailed morphological characterization that will be described in the next section. Their main characteristics are summarized in Table 1.

Table 1. Summary chart with the values of the main features of the Au patterns

Label	NP diameter [nm]	Crystal cut	Λ [µm]	δ [µm]
Pattern I	3.5	*z*-cut	1200	300
Pattern II	170	*z*-cut	1200	300
Pattern III	170	*x*-cut	30	2

4. Morphological characterization of the Au patterns

The morphological characterization of the selected patterns has been carried out at two levels: the micro and the nanoscale. The results are presented in Fig. 3. For the first level, microphotographs have been taken with an upright microscope in reflected light configuration (displayed in the left column of Fig. 3). Note that to show a general overview of the Au-3.5 nm pattern (Pattern I), a macro-image obtained with a system based on a monochrome camera has also shown in Fig. 3(a). For the nanoscale level, especially relevant regarding the plasmonic response, SEM images have been obtained (central column), and the corresponding aggregate size analysis has been performed (right column).
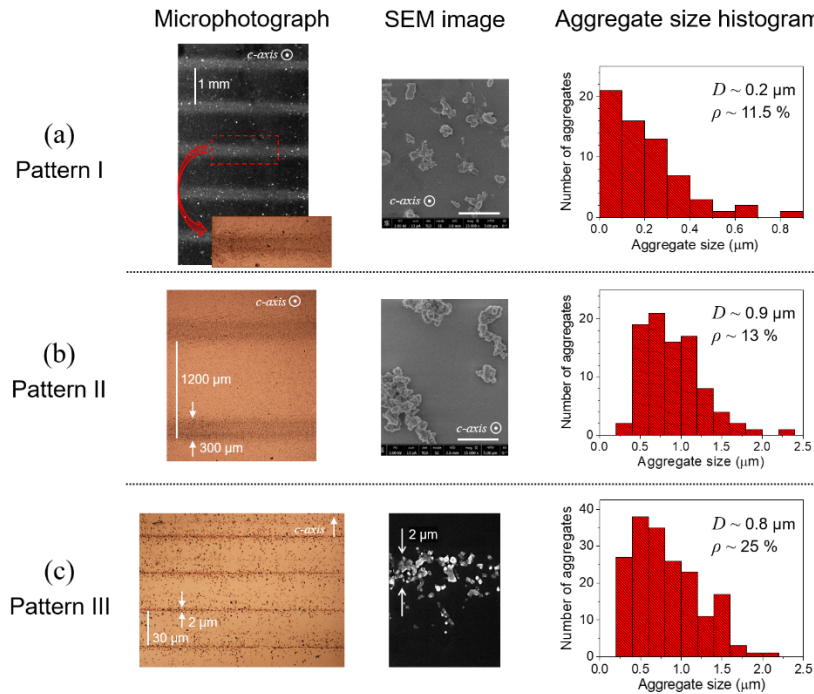

Fig. 3. Microphotographs, SEM images and histograms of the cluster size of fringes patterns with the following features (NP size, crystal cut, Λ, δ): (a) Pattern I (3.5 nm, z-cut, 1200 µm, 300 µm), (b) Pattern II (170 nm, z-cut, 1200 µm, 300 µm), and (c) Pattern III (170 nm, x-cut, 30 µm, 2 µm). In (a) a global image of the pattern with an inset of a fringe is displayed (instead of a microphotograph).

The microphotographs of column-1 exhibit high quality patterns over large areas of the Fe:LiNbO$_3$ crystal surface. These patterns are formed by very well-defined fringes arranged with the same periodicity of the light. Particularly relevant is the result of Fig. 3(a), because this particle pattern is the first one fabricated with PVOT using NPs of dimensions as small as 3.5 nm-diameter, one order of magnitude smaller than previous reported results [40]. Pattern II (Fig. 3(b)) is similar to pattern I at the micrometer level. In both of them, the particles although with different size, cover all the illuminated region formed by fringes with $\delta \sim 300$ µm. This is typical of patterns fabricated in z-cut. Finally, the x-cut Au-170 nm pattern shown in Fig. 3(c), at difference with the previous cases, shows extremely narrow fringes (with $\delta \sim 2$ µm) in comparison with the periodicity of the sinusoidal light pattern (~ 30 µm). These notable differences in the trapping features between z- and x-cut had been already observed [40,43,46] and explain in previous works [47,48]. Briefly, particles tend to get trapped in the minima of the

electric potential energy linked to the superficial PV electric field, and these minima for the *x*-cut configuration under high contrast light patterns are much narrower than for the *z*-cut.

The SEM images show that the fringes are not continuous but assembled by aggregates of arbitrary size and shape. From the analysis of the SEM images, we have extracted the following parameters: average aggregate size *D*, fringe filling factor ρ (i.e., percentage of the fringe area covered by particle/aggregates) and the substrate coverage ratio κ, (i.e., percentage of the substrate surface covered by the particle/aggregates). The values obtained for these parameters are summarized in Table 2.

Table 2. Values of the parameters D, ρ and κ for the three patterns shown in Fig. 3.

Label	D [μm]	ρ [%]	κ [%]
Pattern I	0.2	11.5	2.9
Pattern II	0.8	13	3.2
Pattern III	0.9	25	2.5

The value of *D* obtained for the three cases is notably higher than the nominal size of the NPs in the colloid indicating that the arrangement of the NPs in aggregates has mainly happened during the pattern fabrication procedure. As it can be expected, the two patterns built with the largest NP size (Au 170 nm NPs) show similar values for *D* quite higher than the ones obtained for the pattern built with the 3.5 nm USNPs.

Regarding the fringe filling factor ρ, the pattern fabricated on a *x*-cut substrate (Pattern III), shows a higher value than the other two patterns fabricated on *z*-cut substrates and under similar conditions (Patterns I and II). These results are very likely related with the different thicknesses of the potential energy wells in *x*-cut and *z*-cut configurations, already mentioned. Note that a high value of the parameter ρ indicates a higher metal density inside the fringe and so, a decrease of the distance between nearby aggregates. Finally, the substrate coverage ratio shows appreciable variations depending on the pattern.

5. Characterization of the plasmonic response by reflectance measurements

In order to study the plasmonic behaviour of the metallic micro-patterns shown in Fig. 3, their optical extinction has been characterized in specular reflectance configuration to avoid the contribution of the $Fe:LiNbO_3$ substrate absorption. In Fig. 4, reflectance spectra coming from a representative area of ~ 1 mm^2 of each of the three Au NP patterns are displayed. They have been obtained from the ratio between the reflectance of the $Fe:LiNbO_3$ partially covered by the metallic pattern and the bare $Fe:LiNbO_3$ (reference spectrum).

The overall value of the reflectance can be correlated to the total density of aggregates covering the substrate, measured by the coverage rate, κ (see Table 2). The higher the value of κ, the lower the overall value of the relative reflectance and so, the higher the total amount of extinguished light. Attending to the spectral dependence, the three reflectance curves show a percent drop (that is, an increase of the light extinction) for wavelengths above ~500 nm, which corresponds to the starting of the plasmonic behavior of the structure. This percent drop is more modest in the Au-3.5 nm pattern, but still appreciated in the inset of the spectrum. The drop prompts a broad band that extends to the IR for the two Au-170 nm patterns. Moreover, for these patterns the plasmonic bands have similar width and shape, whereas the resonance of the Au-3.5 nm pattern is considerably narrower. The band peaks are centered at around 625 nm, 640 nm and 655 nm for pattern I, II and III, respectively, i.e., red-shifted in comparison with the LSPR of the NP colloid (see section 2). As it can be expected, these features, i.e. large band width and peak positions, are consistent with the high degree of aggregation and the large aggregate size and dispersion found inside the fringe. In particular, as the aggregate average size *D* increases (0.2 μm, 0.8 μm and 0.9 μm for patterns I, II and III, respectively) the plasmonic band peak shifts to longer
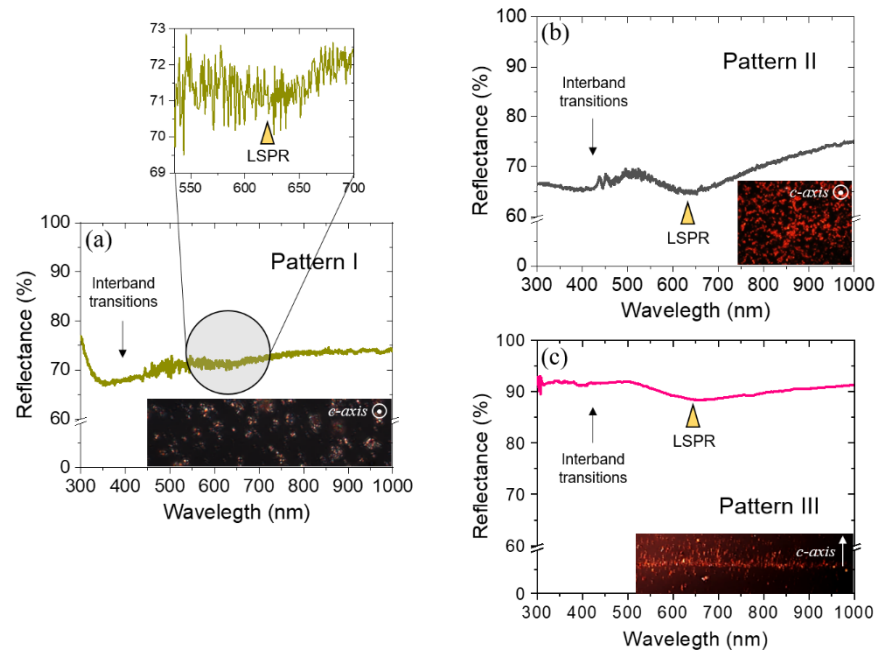
Fig. 4. Reflectance spectra of the optical extinction obtained for the three Au patterns shown in Fig. 3: (a) Pattern I (including an inset of the plasmonic band), (b) Pattern II, and (c) Pattern III. In the right corner of the three spectra, micro-images with high magnification obtained in polarized reflected light configuration are displayed.

wavelengths. These kind of metallic aggregates with plasmonic properties are commonly called in the literature as disordered plasmonic networks (DPNs) [19]. Finally, it is worth mentioning that at short wavelengths one can observe interband transitions, indicated in the figure, that are close but separated from the plasmonic bands.

The extinction reflectance measurements inform about the regions of the optical spectrum in which we should expect plasmonic effects. However, the light extinction by a metallic structure is the sum of the light absorbed and scattered, being only the second contribution relevant for our purposes of FL enhancement. A high scattering cross section is related with a huge increase of the electric field magnitude and its confinement in the nanometric surroundings of the metallic NPs or aggregates, leading to the enhancement of optical phenomena such as FL emission. Then, the reflectance measurements showed above do not allow us to completely predict the suitability of these plasmonic platforms as efficient scatters. To provide some qualitative information of this latter aspect, we have complemented the spectral characterization with polarized reflected light microphotographs corresponding to the inner area of a pattern fringe, shown in the right bottom corners of Fig. 4. The use of two crossed polarizers, allows the collection of just the scattered light coming from the particles. The images of the two Au-170 nm patterns show yellow-reddish features (in accordance with the plasmonic response observed in Fig. 4) over a black background (the Fe:LiNbO$_3$ surface), while the image from the Au-3.5 nm pattern shows a notably lower scattered light level. These results agree with the well-known fact that large NPs and aggregates tend to be efficient scatters, whereas most of the light extinguished by the small NPs is caused by absorption processes [12].

6.   Application to fluorescence enhancement

From the previous spectral analysis, we can conclude that the patterns with the largest NP size should become more suitable for exploring and exploiting the enhancement of optical properties in the red region of the spectrum. Therefore, the Au-170 nm patterns will be mostly employed for the upcoming experiments.

6.1.   Plasmonic enhancement of fluorescence of Rhodamine B dye

In order to test the plasmonic capabilities of the Au-170 nm patterns for improving FL the emission properties of a nearby dye, we should select a suitable fluorochrome whose excitation and/or emission bands overlap with the plasmonic response. We have chosen Rhodamine B (RB) that presents a good overlapping with the plasmonic band of Au-patterns for both the excitation and emission spectra, shown in Fig. 5. RB is a fluorescent dye with a high quantum efficiency [49], very popular for labeling in applications of biotechnology [13]. To place a homogenous layer containing the RB molecules onto the Au NP patterns, the patterned substrate was immersed in a solution of ethanol containing the fluorescent molecules for a few seconds.
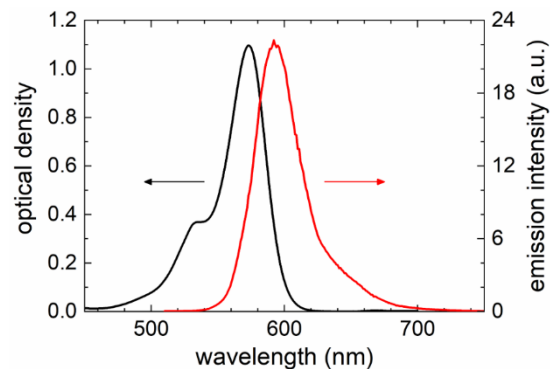

Fig. 5. Excitation (black) and emission (red) spectra of RB dye in ethanol. The emission spectrum has been obtained exciting at $\lambda_{exc} = 500$ nm.

First, we will test Au-170 nm patterns II and III fabricated on z- and x-cut respectively, and with different morphological and spectral features described in sections 4 and 5. The FL emission of the RB layer covering the Au patterns has been characterized by widefield FL microscopy ($\lambda_{exc} = 550$ nm). The upper part of Fig. 6 shows the FL microphotographs of a representative area of each Au pattern. The FL images reveal a reddish light, with the highest level of intensity coming from the patterned area with the NP aggregates. This means that the Au NP aggregates are playing a positive impact on the FL emission of the RB. Although the FL intensity coming from the inter-fringe area is very low, there is still a non-negligible FL signal due to a residual background of particles and aggregates placed out of the fringes.

To quantify the influence of the Au patterns on the dye fluorescence, we have measured the magnitude of the FL enhancement, defined as the ratio of the FL signal in the presence and in the absence of the metallic structure. Specifically, we have obtained the average FL enhancement profile of the RB along the perpendicular direction to the fringes for the whole metallic platform. To this end, quantitative image analysis through the open-source software ImageJ has been used. We averaged the whole set of 1-pixel line intensity profiles and normalized them by a reference FL intensity value, taken from a metal-free area of the RB layer. The resulting FL enhancement profiles, plotted in Fig. 6 (below the corresponding FL image), show the same shape, periodicity and fringe thickness of the particle pattern. To characterize with a single parameter the platform plasmonic behavior, we have defined the FL enhancement factor (FEF) as the average of the
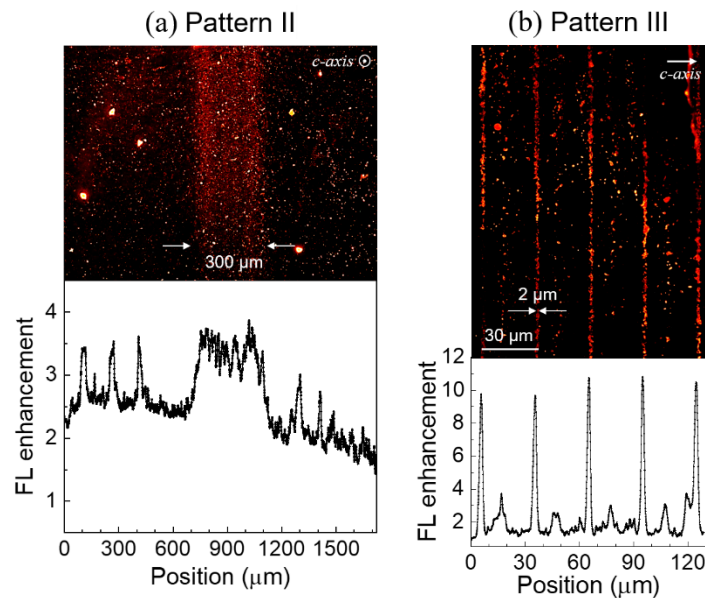
Fig. 6. FL images and the corresponding average FL enhancement profiles along the perpendicular direction to the fringes for three Au 170 nm fringe patterns with different features (crystal cut, Λ, δ): (a) Pattern II (*z*-cut, 1200 µm, 300 µm), and (b) Pattern III (*x*-cut, 30 µm, 2 µm). The FL images have been obtained exciting at 550 nm.

maximum values of the FL enhancement profile. This parameter takes a relevant value of 3.7 for Pattern II, and a significantly higher value of 10 for Pattern III. At this point, one can wonder about the origin of the significantly higher FEF of pattern III fabricated on *x*-cut compared to pattern II on *z*-cut. Being aware that both patterns are assembled with nanoparticles of the same size, this result is very likely due to the substantially higher fringe filling factor ρ (see Table 2) for the *x*-cut pattern, which maximizes the metal density around the RB molecules.

In summary, we have obtained a successful FL enhancement behavior for these Au plasmonic platforms fabricated by PVOT from 170 nm nanoparticles. The results indicate that the main features supporting this remarkable FL enhancement are: i) the broad plasmonic response of the Au aggregates that allows the overlapping with both, the excitation and emission bands of the RB, having a positive impact in the excitation rate and quantum efficiency of the dye; ii) the high metal aggregate density around the dye molecules, i.e. a high fringe filling factor.

Last, the suitability of the Au-3.5 nm patterns for enhancing the FL emission of the RB was also tested. It has been found a quite modest but significant enhancement with a FEF of 1.2. Despite the low scattering cross-section expected for USNPs with such a small size, the capability of the PVOT to assemble patterns with a substructure of aggregates may contribute to obtain this non negligible enhancement in the visualization of the RB layer.

6.2. Fluorescence enhancement in DNA tagged with Rhodamine B

Finally, complementary experiments to show the potential for biomedical imaging have been carried out. For this purpose, we have employed RB tagged DNA probes in an aqueous solution that have been deposited on 170 nm DPN patterns fabricated onto the *x*-cut Fe:LiNbO$_3$ substrates. This kind of DNA probes is typically used in FISH experiments to visualize DNA sequences (gens, etc.) [50]. In order to approach the DNA molecules to the Au pattern, a droplet of 0.5 µL containing the RB tagged DNA on an aqueous solution was deposited on top of the pattern.

The volume of the droplet is similar to the one typically used in biological assays. After that, we placed a cover slide over the RB layer in order to get a homogeneous distribution of the dye on top of the Au pattern. To rise the amount of Au Np aggregates surrounding the DNA molecules, we increased the density of NPs in the colloid with regard to the previous experiments.

The upper part of the Fig. 7 shows the corresponding FL image of a pattern obtained by sinusoidal illumination with a 25-μm period of an *x*-cut substrate. Below the microphotograph the FL enhancement profile, calculated in the same way as in previous sections, is plotted. Again, the fringe area with the Au DPNs shows an intense red FL signal following the periodicity of the metallic pattern whereas the signal coming from the inter-fringe area is negligible. In other words, without using the plasmonic platform as slide the FL DNA signal would not be observed. In this case, the FL enhancement factor is around 3. It is notable although lower than the FEF shown in previous experiments when the RB is directly deposited on the substrate. Note that, the good overlap between the plasmonic resonance and the excitation and emission RB bands have contributed to this notable FEF. In fact, we have also tested the FL enhancement of DNA probes tagged with other dyes as DAPI (UV excitation and blue emission) and fluorescein (blue excitation and green emission). By contrast with the case of Rhodamine B, those dyes did not display almost any enhancement in their FL signal because of the poor spectral overlapping of the plasmonic band with the excitation and FL emission bands of those dyes.
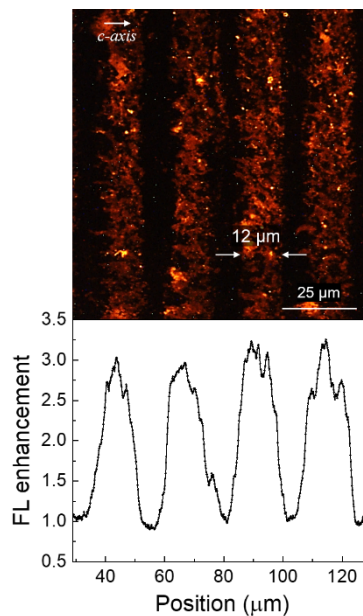

Fig. 7. FL microscope image of a layer of RB tagged DNA placed on top of an Au fringe pattern with the features of (170 nm, *x*-cut, 25 μm, 12 μm). Under the image, the corresponding average FL enhancement profile of the RB layer is shown. The FL image has been obtained by exciting with $\lambda_{exc} = 550$ nm in FL widefield microscopy configuration.

7. Conclusion

In this work, we report for the first time the manipulation and assembling of Au NPs into periodic micro-patterns by photovoltaic optoelectronic tweezers to use them as fluorescence enhancer platforms. Two markedly different Au NP diameters, 170 and 3.5 nm (ultra-small particles), has been employed. From both NP sizes, fringe patterns with high homogeneity at the microscale and

with different periodicity and fringe thickness (down to a very few μm) have been successfully obtained over large active areas (up to 1 cm^2). It is worthwhile remarking that PVOT have successfully assembled for the first time the USNPs with sizes as small as d ~ 3.5 nm, one order of magnitude smaller than the previous reported smallest values (25 nm) [42]. The fringes that build the patterns exhibit a sub-structure of aggregates, whose features have demonstrated to be closely related to the crystal orientation (*x*- or *z*-cut) and the visibility (contrast) of the light illumination profile.

When applying the Au patterns as FL enhancer platforms, those assembled from 170 nm NP aggregates have shown much better performance than the ones obtained from USNPs. They present broad plasmonic bands extended from the visible to the NIR range and the highest level of scattered light. When employing standalone Rhodamine B molecules, the Au-170 nm platforms have revealed FL enhancement factors as great as 10. In turn, when the RB molecules were acting as DNA taggers, the observed FL increase was 3-fold. These remarkable FL enhancement factors have been prompted by: i) the advantageous overlapping between the plasmonic bands of the metallic structure and the excitation and emission band of the dye, and ii) the high density of aggregates inside the fringes, i.e. the high filling factor ρ. These properties make the patterns obtained on *x*-cut substrates under sinusoidal high contrast illumination the most efficient as FL enhancer platforms.

In conclusion, the PVOT technique has been demonstrated to be a flexible, cost-effective, and suitable tool to fabricate very efficient Au FL enhancer platforms with large active areas, whose efficient operation is based on their plasmonic effects. The very broad plasmonic responses could be useful for working with fluorochromes of different spectral bands. They are particularly valuable in the field of biomedicine due to the inert behavior of the Au NPs and the ease to be functionalized. In addition, the possibility to trap and arrange NPs of very small sizes could also pave the way to the field of fabricating nanometric heaters [51].

Disclosures. The authors declare that there are no conflicts of interest related to this article.

Data availability. Data underlying the results presented in this paper are not publicly available at this time but may be obtained from the authors upon reasonable request.

References

1. E. A. Coronado, E. R. Encina, and F. D. Stefani, "Optical properties of metallic nanoparticles: manipulating light, heat and forces at the nanoscale," Nanoscale **3**(10), 4042–4059 (2011).
2. J. A. Scholl, A. L. Koh, and J. A. Dionne, "Quantum plasmon resonances of individual metallic nanoparticles," Nature **483**(7390), 421–427 (2012).
3. K. M. Mayer and J. H. Hafner, "Localized surface plasmon resonance sensors," Chem. Rev. **111**(6), 3828–3857 (2011).
4. N. Pelton, J. Aizpurua, and G. Bryant, "Metal-nanoparticle plasmonic," Laser Photonics Rev. **2**(3), 136–159 (2008).
5. Q. Ruan, L. Shao, Y. Shu, J. Wang, and H. Wu, "Growth of monodisperse gold nanospheres with diameters from 20 nm to 220 nm and their core/satellite nanostructures," Adv. Opt. Mater. **2**(1), 65–73 (2014).
6. X. Huang, P. K. Jain, I. H. El-Sayed, and M. A. El-Sayed, "Plasmonic photothermal therapy (PPTT) using gold nanoparticles," Lasers Med. Sci. **23**(3), 217–228 (2008).
7. Y. Jin, "Engineering plasmonic gold nanostructures and metamaterials for biosensing and nanomedicine," Adv. Mater. **24**(38), 5153–5165 (2012).
8. G. González-Rubio, P. Díaz-Núñez, A. Rivera, A. Prada, G. Tardajos, J. González-Izquierdo, L. Bañares, P. Llombart, L. G. Macdowell, M. Alcolea Palafox, L. M. Liz-Marzán, O. Peña-Rodríguez, and A. Guerrero-Martínez, "Femtosecond laser reshaping yields gold nanorods with ultranarrow surface plasmon resonances," Science **358**(6363), 640–644 (2017).

9. R. A. Sperling, P. R. Gil, F. Zhang, M. Zanella, and W. J. Parak, "Biological applications of gold nanoparticles," Chem. Soc. Rev. **37**(9), 1896–1908 (2008).

10. G. Baffou and R. Quidane, "Thermo-plasmonic: using metallic nanostructures as nano-sources of heat," Laser Photonics Rev. **7**(2), 171–187 (2013).

11. M. R. K. Ali, Y. M. Wu, and A. El-Sayed, "Gold-nanoparticle-assisted plasmonic photothermal therapy advances toward clinical application," J. Phys. Chem. C **123**(25), 15375–15393 (2019).

12. S. A. Maier, *Plasmonics: fundamentals and applications*, (Springer, 2007).

13. F. Tam, G. P. Goodrich, B. R. Johnson, and N. J. Halas, "Plasmonic enhancement of molecular fluorescence," Nano Lett. **7**(2), 496–501 (2007).

14. J. Langer, D. Jimenez de Aberasturi, and J. Aizpurua, *et al.*, "Present and future of surface-enhanced Raman scattering," ACS Nano **14**(1), 28–117 (2020).

15. Q. Luo, C. Zhang, X. Deng, H. Zhu, Z. Li, Z. Wang, X. Chen, and S. Huang, "Plasmonic effects of metallic nanoparticles on enhancing performance of perovskite solar cells," ACS Appl. Mater. Interfaces **9**(40), 34821–34832 (2017).

16. L. Sánchez-García, C. Tserkezis, M. O. Ramírez, P. Molina, J. J. Carvajal, M. Aguiló, F. Díaz, J. Aizpurua, and L. E. Bausá, "Plasmonic enhancement of second harmonic generation from nonlinear RbTiOPO$_4$ crystals by aggregates of silver nanostructures," Opt. Express **24**(8), 8491–8500 (2016).

17. S. Keren-Zur, O. Avayu, L. Michaeli, and T. Ellenbogen, "Nonlinear beam shaping with plasmonic metasurfaces," ACS Photonics **3**(1), 117–123 (2016).

18. A. Gómez-Tornero, C. Tserkezis, L. Mateos, L. E. Bausá, and M. O. Ramírez, "2D arrays of hexagonal plasmonic necklaces for enhanced second harmonic generation," Adv. Mater. **29**(15), 1605267 (2017).

19. A. Sanchot, G. Baffou, R. Marty, A. Arbouet, R. Quidant, C. Girard, and E. Dujardin, "Plasmonic nanoparticle networks for light and heat concentration," ACS Nano **6**(4), 3434–3440 (2012).

20. Z. Yan, M. Sajjan, and N. F. Scherer, "Fabrication of a material assembly of silver nanoparticles using the phase gradients of optical tweezers," Phys. Rev. Lett. **114**(14), 143901 (2015).

21. M. Horák, K. Bukvišová, V. Švarc, J. Jaskowiec, V. Křápek, and T. Šikola, "Comparative study of plasmonic antennas fabricated by electron beam and focused ion beam lithography," Sci. Rep. **8**(1), 9640 (2018).

22. C. Farcau, D. Marconi, A. Colniță, I. Brezeștean, and L. Barbu-Tudoran, "Gold nanopost-shell arrays fabricated by nanoimprint lithography as a flexible plasmonic sensing platform," Nanomaterials **9**(11), 1519 (2019).

23. S. Y. Lu, H. L. Chen, K. H. Wu, and Y. Y. Chen, "Formation of nanowire striations driven by Marangony instability in spin-cast polymer thin films," Langmuir **23**(20), 10069–10073 (2007).

24. H. Ma, R. Dong, J. D. Van Horn, and J. Hao, "Spontaneous formation of radially aligned microchannels," Chem. Commun. **47**(7), 2047–2049 (2011).

25. T. E. Tesema, R. McFarland-Porter, E. Zerai, J. Grey, and T. G. Habteyes, "Hierachical self-assembly and chemical imaging of nanoscale domains in polymer blend thin films," J. Phys. Chem. C **126**(17), 7764–7772 (2022).

26. M. Carrascosa, A. García-Cabañes, M. Jubera, J. B. Ramiro, and F. Agulló-López, "LiNbO$_3$: A photovoltaic substrate for massive parallel manipulation and patterning of nano-objects," Appl. Phys. Rev. **2**(4), 040605 (2015).

27. A. García-Cabañes, A. Blázquez-Castro, L. Arizmendi, F. Agulló-López, and M. Carrascosa, "Recent achievements on photovoltaic optoelectronic tweezers based on lithium niobate," Crystals **8**(2), 65 (2018).

28. C. Sebastián-Vicente, E. Muñoz-Cortés, A. García-Cabañes, F. Agulló-López, and M. Carrascosa, "Real-time operation of photovoltaic optoelectronic tweezers: new strategies for massive nano-object manipulation and reconfigurable patterning," Part. Part. Syst. Charact. **36**(9), 1900233 (2019).

29. J. F. Muñoz-Martínez, J. B. Ramiro, A. Alcázar, A. García-Cabañes, and M. Carrascosa, "Electrophoretic versus dielectrophoretic nanoparticle patterning using optoelectronic tweezers," Phys. Rev. Appl. **7**(6), 064027 (2017).

30. H. A. Eggert, F. Y. Kuhnert, K. Buse, J. R. Adleman, and D. Psaltis, "Trapping of dielectric particles with light-induced space-charge fields," Appl. Phys. Lett. **90**(24), 241909 (2007).

31. X. Zhang, J. Wang, B. Tang, X. Tan, R. A. Rupp, L. Pan, Y. Kong, Q. Sun, and J. Xu, "Optical trapping and manipulation of metallic micro/nanoparticles via photorefractive crystals," Opt. Express **17**(12), 9981–9988 (2009).

32. M. Jubera, I. Elvira, A. García-Cabañes, J. L. Bella, and M. Carrascosa, "Trapping and patterning of biological objects using photovoltaic tweezers," Appl. Phys. Lett. **108**(2), 023703 (2016).

33. I. Elvira, J. F. Muñoz-Martínez, A. Barroso, C. Denz, J. B. Ramiro, A. García-Cabañes, F. Agulló-López, and M. Carrascosa, "Massive ordering and alignment of cylindrical micro-objects by photovoltaic optoelectronic tweezers," Opt. Lett. **43**(1), 30–33 (2018).

34. C. Sebastián-Vicente, P. Remacha-Sanz, E. Elizechea-López, A. García-Cabañes, and M. Carrascosa, "Combinatorial nanoparticle patterns assembled by photovoltaic optoelectronic tweezers," Appl. Phys. Lett. **121**(12), 121104 (2022).

35. M. Esseling, A. Zaltron, C. Sada, and C. Denz, "Charge sensor and particle trap based on z-cut lithium niobate," Appl. Phys. Lett. **103**(6), 061115 (2013).

36. M. Esseling, A. Zaltron, W. Horn, and C. Denz, "Optofluidic droplet router," Laser Photonics Rev. **9**(1), 98–104 (2015).

37. J. F. Muñoz-Martínez, M. Jubera, J. Matarrubia, A. García-Cabañes, F. Agulló-López, and M. Carrascosa, "Diffractive optical devices produced by light-assisted trapping of nanoparticles," Opt. Lett. **41**(2), 432–435 (2016).

38. X. Zhang, E. R. Mugisha, Y. Mi, X. Liu, M. Wang, Z. Gao, K. Gao, L. Shi, H. Chen, and W. Yan, "Photovoltaic cycling to-and-fro actuation of a water-microdroplet for automatic repeatable solute acquisition on oil-infused hydrophobic LN:Fe surface," ACS Photonics **8**(2), 639–647 (2021).

39. A. Puerto, J. L. Bella, C. López Fernández, A. García-Cabañes, and M. Carrascosa, "Optoelectronic manipulation of bio-droplets containing cells or macromolecules by active ferroelectric platforms," Biomed. Opt. Express **12**(10), 6601–6613 (2021).

40. I. Elvira, J. F. Muñoz-Martínez, M. Jubera, A. García-Cabañes, J. L. Bella, P. Haro-González, M. A. Díaz-García, F. Agulló-López, and M. Carrascosa, "Plasmonic enhancement in the fluorescence of organic and biological molecules by photovoltaic tweezing assembly," Adv. Mater. Technol. **2**(8), 1700024 (2017).

41. D. Zhang, B. Gokce, and S. Barcikowski, "Laser synthesis and processing of colloids: fundamentals and applications," Chem. Rev. **117**(5), 3990–4103 (2017).

42. C. Doñate-Buendía, M. Fernández-Alonso, J. Lancis, and G. Mínguez-Vega, "Overcoming the barrier of nanoparticle production by femtosecond laser ablation in liquids using simultaneous spatial and temporal focusing," Photonics Res. **7**(11), 1249–1257 (2019).

43. C. Deraedt, L. Salmon, S. Gatard, R. Ciganda, R. Hernandez, J. Ruiz, and D. Astruc, "Sodium borohydride stabilizes very active gold nanoparticle catalysts," Chem. Commun. **50**(91), 14194–14196 (2014).

44. M. N. Martin, J. I. Basham, P. Chando, and S. K. Eah, "Charged gold nanoparticles in non-polar solvents: 10-min synthesis and 2D self-assembly," Langmuir **26**(10), 7410–7417 (2010).

45. J. F. Muñoz-Martínez, I. Elvira, M. Jubera, A. García-Cabañes, J. B. Ramiro, C. Arregui, and M. Carrascosa, "Efficient photo-induced dielectrophoretic particle trapping on Fe:LiNbO₃ for arbitrary two dimensional patterning," Opt. Mater. Express **5**(5), 1137–1146 (2015).

46. J. Matarrubia, A. García-Cabañes, J. L. Plaza, F. Agulló-López, and M. Carrascosa, "Optimization of particle trapping and patterning via photovoltaic tweezers: role of light modulation and particle size," J. Phys. D: Appl. Phys. **47**(26), 265101 (2014).

47. C. Arregui, J. B. Ramiro, A. Alcázar, A. Méndez, H. Burgos, A. García-Cabañes, and M. Carrascosa, "Optoelectronic tweezers under arbitrary illumination patterns: theoretical simulations and comparison to experiment," Opt. Express **22**(23), 29099–29110 (2014).

48. J. F. Muñoz-Martínez, A. Alcázar, and M. Carrascosa, "Time evolution of photovoltaic fields generated by arbitrary light patterns in z-cut LiNbO₃:Fe: application to optoelectronic nanoparticle manipulation," Opt. Express **28**(12), 18085–18102 (2020).

49. F. L. Arbeloa, P. R. Ojeda, and I. L. Arbeloa, "Flourescence self-quenching of the molecular forms of Rhodamine B in aqueous and ethanolic solutions," J. Lumin. **44**(1-2), 105–112 (1989).

50. L. T. C. França, E. Carrilho, and T. B. L. Kist, "A review of DNA sequencing techniques," Q. Rev. Biophys. **35**(2), 169–200 (2002).

51. D. Wang, Y. R. Koh, Z. A. Kudyshev, K. Maize, A. V. Kildishev, A. Boltasseva, V. M. Shalaev, and A. Shakouri, "Spatial and temporal nanoscale plasmonic heating quantified by thermoreflectance," Nano Lett. **19**(6), 3796–3803 (2019).